Ray-tracing simulations of whistler-mode wave propagation in different rescaled dipole magnetic fields

YangGuang Ke[1,2,3], QuanMing Lu[1,2,3*], XinLiang Gao[1,2,3*], HuaYue Chen[1,2,3], and Rui Chen[1,2,3]

[1]CAS Key Laboratory of Geoscience Environment, School of Earth and Space Sciences, University of Science and Technology of China, Hefei 230026, China;

[2]CAS Center for Excellence in Comparative Planetology, Hefei 230026, China;

[3]Collaborative Innovation Center of Astronautical Science and Technology, Harbin 150001, China

Key Points:
- A ray-tracing code is developed to study the propagation of whistler-mode waves in different rescaled dipole magnetic fields.
- Parallel whistler waves at higher frequencies tend to have larger wave normal angles after leaving the magnetic equator.
- The wave raypath and wave normal remain the same, whereas the wave gain is smaller in a scaled-down dipole field.

Citation: Ke, Y. G., Lu, Q. M., Gao, X. L., Chen, H. Y., and Chen, R. (2022). Ray-tracing simulations of whistler-mode wave propagation in different rescaled dipole magnetic fields. *Earth Planet. Phys.*, 6(6), 555–562. http://doi.org/10.26464/epp2022048

Abstract: Kinetic simulation is a powerful tool to study the excitation and propagation of whistler-mode waves in the Earth's inner magnetosphere. This method typically applies a scaled-down dipole magnetic field to save computational time. However, it remains unknown whether whistler wave propagation in the scaled-down dipole field is consistent with that in the realistic dipole field. In this work, we develop a ray-tracing code with a scalable dipole magnetic field to address this concern. The simulation results show that parallel whistler waves at different frequencies gradually become oblique after leaving the equator and propagate in different raypaths in a dipole magnetic field. During their propagation, the higher frequency waves tend to have larger wave normal angles at the same latitude. Compared with the wave propagation in a realistic dipole field, the wave raypath and wave normal remain the same, whereas the wave amplification or attenuation is smaller because of the shorter propagation time in a scaled-down dipole field. Our study provides significant guidance for kinetic simulations of whistler-mode waves.

Keywords: whistler wave; ray tracing; propagation; dipole magnetic field; magnetosphere

1. Introduction

Whistler-mode waves are ubiquitous in the Earth's inner magnetosphere. Outside the plasmasphere, they are narrowband and coherent electromagnetic emissions (Burtis and Helliwell, 1969; Tsurutani and Smith, 1974, 1977; Li W et al., 2012), whereas in the plasmasphere or plume, they are typically broadband and incoherent and are known as a plasmaspheric hiss (Thorne et al., 1973; Chan and Holzer, 1976; Meredith et al., 2018; Su ZP et al., 2018). The narrowband and coherent whistler waves, known as chorus waves, exhibit hiss-like emissions or discrete elements that usually appear as repetitive rising or falling tones (Burtis and Helliwell, 1976; Li W et al., 2012; Gao XL et al., 2014, 2022; Lu QM et al., 2021). They are typically observed over a frequency range of $0.1-0.8\ f_{ce}$ (where f_{ce} is the equatorial electron cyclotron frequency), often divided by a power gap at $0.5\ f_{ce}$ into lower band ($0.1-0.5\ f_{ce}$) and upper band ($0.5-0.8\ f_{ce}$; Tsurutani and Smith, 1974; Li W et al., 2011; Gao XL et al., 2019; Sauer et al., 2020; Chen HY et al., 2021,

2022). Whistler waves are generally excited near the magnetic equator (LeDocq et al., 1998; Santolík et al., 2005; Li W et al., 2013) and are driven by anisotropic energetic electrons injected from the plasma sheet (Kennel and Petschek, 1966; Anderson and Maeda, 1977; Li W et al., 2009). Furthermore, quasi-parallel whistler waves predominate in the equatorial source regions (Agapitov et al., 2013; Li W et al., 2013). As a primary candidate for accelerating electrons to form the electron radiation belt (Horne and Thorne, 1998; Horne et al., 2005; Reeves et al., 2013; Thorne et al., 2013) and precipitating electrons to produce pulsating and diffuse auroras (Ni BB et al., 2008; Nishimura et al., 2010; Thorne et al., 2010; Kasahara et al., 2018), whistler-mode waves have been widely investigated through observations and numerical simulations.

Kinetic simulations, especially particle-in-cell (PIC) simulations, are powerful tools to study the excitation and propagation of whistler-mode waves in the Earth's inner magnetosphere. A number of one-dimensional (1-D) kinetic simulations in a scaled-down dipole magnetic field (or a mirror field) have been carried out to better understand the generation of the whistler-mode chorus (Katoh and Omura, 2007; Omura et al., 2008; Tao X et al., 2020). These simulation works suggest that because of the phase space variation of resonant electrons, the resonant currents contribute to the

nonlinear growth of the whistler-mode chorus (Katoh and Omura, 2006; Hikishima and Omura, 2012; Nunn and Omura, 2012). Moreover, the threshold and optimal amplitude conditions for nonlinear growth of the rising-tone chorus (Omura et al., 2009; Omura and Nunn, 2011) have been confirmed by 1-D kinetic simulations (Hikishima and Omura, 2012). In recent years, two-dimensional (2-D) kinetic simulations in a scaled-down dipole field (or a mirror field) have also been performed to study both the excitation and propagation of whistler-mode waves (Ke YG et al., 2017, 2021; Da Silva et al., 2017; Lu QM et al., 2019). These simulations indicate that whistler-mode waves are generally excited near the equator with the quasi-parallel wave normal and gradually become oblique during propagation toward high latitudes, consistent with statistical observations (Agapitov et al., 2011; Li W et al., 2011; Artemyev et al., 2016). Furthermore, the observed propagation properties of whistler waves in the density ducts have been reproduced by 2-D kinetic simulations (Ke YG et al., 2021) and have exhibited quasi-parallel propagation.

Both 1-D and 2-D kinetic simulations of whistler waves typically apply a scaled-down dipole field to reduce the computational time. Although these simulations contribute a great deal to understanding the evolution of whistler waves, the similarities and differences between wave propagation in a scaled-down dipole field and a realistic dipole field remain unknown. To address this question, we developed a ray-tracing code with a scalable dipole magnetic field to study whistler wave propagation. The ray-tracing technique is a common approach that has been used extensively to study the propagation of plasma waves in the Earth's magnetosphere (Horne, 1989; Bortnik et al., 2008; Chen LJ et al., 2009; Xiao FL et al., 2016; Guo MY et al., 2020; Kang N et al., 2021; Deng ZK et al., 2022). The ray-tracing model is introduced in Section 2, and the simulation results are shown in Section 3. In Section 4, we summarize and discuss the primary conclusions of this study.

2. Ray-Tracing Model

A 2-D ray-tracing code with a scalable dipole magnetic field was developed to investigate the propagation of whistler-mode waves in different rescaled dipole magnetic fields. This ray-tracing code numerically calculates the wave raypath by solving the Haselgrove equations (Haselgrove, 1955; Kimura, 1966). The cold plasma dispersion relation (Stix, 1992) is used in the ray-tracing model because the background plasma in the Earth's inner magnetosphere is at lower temperatures in the range of several electron volts (Décréau et al., 1982). The cold plasma approximation is valid when the phase velocities of the waves are larger than the thermal velocity of the background plasma, and that condition is satisfied in this study. The wave growth or damping can be evaluated by integrating the local growth rate γ along the wave raypath:

$$B_w = B_{w0}\exp\left(\int_0^t \gamma \mathrm{d}t\right), \tag{1}$$

where B_w is the wave amplitude after a period of propagation, proportional to the initial wave amplitude B_{w0}. The growth rate γ is required to be much smaller than the wave frequency, $\gamma \ll \omega$, which is valid in our simulations. The plasma is assumed to consist of cold electrons and protons and rare hot electrons. The growth

rate γ can be calculated by using a common approach (Kennel, 1966; Brinca, 1972) applied widely in previous works (Bortnik et al., 2003, 2008; Chen LJ et al., 2010; Kang N et al., 2021), based on a given hot electron distribution. In the present study, we estimated the growth rate γ by considering the contributions of only the fundamental cyclotron resonance and the Landau resonance. Therefore, the growth rates obtained in our code and given by the WHAMP (waves in homogeneous, anisotropic, multicomponent plasmas) model (Rönnmark, 1982) are almost, but not quite, equivalent. Furthermore, the validity of our ray-tracing code was confirmed by comparing our ray-tracing results with those of the Python-based ray tracer (Kang N et al., 2021).

2.1 Scalable Dipole Magnetic Field and Density Model

The background magnetic field in the Earth's inner magnetosphere is approximately a dipole magnetic field. A scalable dipole magnetic field used in the simulation system can be described as

$$\begin{cases} B_r = -B_0 \cdot 2\sin\lambda/(\eta r)^3, \\ B_\lambda = B_0 \cdot \cos\lambda/(\eta r)^3, \\ B_c = \left(B_r^2 + B_\lambda^2\right)^{1/2}, \end{cases} \tag{2}$$

where λ is the magnetic latitude and r is the radial distance of a certain point to the Earth's center in units of Earth radius R_E. Components B_r and B_λ are the radial and tangential components of the total magnetic field B_c, and $B_0 = 31,200$ nT is the equatorial magnetic field strength at the Earth's surface. Different rescaled dipole fields can be obtained by changing the scaling factor η. A realistic dipole field corresponds to $\eta = 1$ and a scaled-down dipole field has $\eta > 1$. Three different rescaled dipole fields are used in our simulation models: Models 1 ($\eta = 1$), 2 ($\eta = 2$), and 3 ($\eta = 6$). The simulation domain of $L = 5$–7 in Model 1 corresponds to the domain of $L = 2.5$–3.5 in Model 2 and the domain of $L = 5/6$–7/6 in Model 3, where $L = r/(\cos\lambda)^2$ is the L-shell. The corresponding latitude ranges in the three models are the same (see Figure 1).

The background plasma density in the simulation system follows an empirical model of the plasma trough density,

$$\begin{cases} n_e = n_{eq}(\cos\lambda)^{-2\alpha}, \\ n_{eq} = \left(n_0(\eta L)^{-4.5} + 1 - \exp\left[0.2 - 0.1\,(\eta L)\right]\right)\mathrm{cm}^{-3}, \end{cases} \tag{3}$$

which combines a field-aligned density model (Denton et al., 2002, 2006) and an equatorial density model (Carpenter and Anderson, 1992). The equatorial electron density n_{eq} is assumed to be 5 cm^{-3} at $L = 6$ in the realistic dipole field ($\eta = 1$), giving $n_0 = 14,826$. For simplicity, the constant density n_e along a magnetic field line ($\alpha = 0$) is applied, which is commonly used in PIC simulations (Katoh and Omura, 2006; Lu QM et al., 2019; Ke YG et al., 2020). The scaling factor η in Equations (2) and (3) ensures that the magnetic field strength B_c and the electron density n_e remain the same at the corresponding locations in the different rescaled dipole fields. The distributions of the magnetic field strength B_c and the plasma density n_e in the simulation domains of the three models are shown in Figure 1.

2.2 Hot Electron Distribution

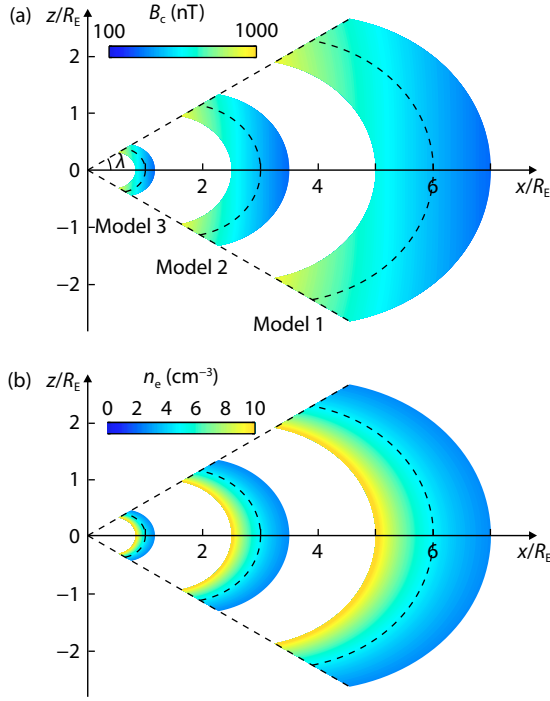For simplicity, the hot electron distribution is assumed to be a bi-

Figure 1. The distributions of (a) the background magnetic fields and (b) the electron densities in the three models.

Maxwellian distribution:

$$f\left(v_{\parallel}, v_{\perp}, \lambda\right) = \frac{n_h}{(2\pi)^{2/3} v_{\text{th}\parallel} v_{\text{th}\perp}^2} \exp\left(-\frac{v_{\parallel}^2}{2v_{\text{th}\parallel}^2} - \frac{v_{\perp}^2}{2v_{\text{th}\perp}^2/\zeta(\lambda)}\right), \quad (4)$$

where n_h and $v_{\text{th}\parallel}$ ($v_{\text{th}\perp}$) are the number density and the parallel (perpendicular) thermal velocity of hot electrons at the magnetic equator, and $v_{\parallel}$ ($v_{\perp}$) is the parallel (perpendicular) electron velocity. Along the magnetic field lines, the hot electron distribution satisfies Liouville's theorem (Summers et al., 2012; Lu QM et al., 2019), giving $\zeta(\lambda) = 1 + \left(T_{h\parallel}/T_{h\perp} - 1\right)\left(1 - B_{eq}/B_c(\lambda)\right)$. Here, $T_{h\parallel}$ ($T_{h\perp}$) is the parallel (perpendicular) temperature of hot electrons at the equator and B_{eq} is the equatorial magnetic field strength equal to $B_c(\lambda = 0)$.

3. Simulation Results

A series of ray-tracing simulations were performed to study the propagation of whistler-mode waves in different rescaled dipole fields. The different-frequency whistler waves with the parallel wave normal were launched at the equator at $L = 6$ in Model 1, $L = 3$ in Model 2, and $L = 1$ in Model 3. In this work, we studied the wave propagation only in the latitude range of $\lambda \leq 30°$ because most whistler waves are observed within this range.

3.1 Wave Raypath and Wave Normal

Figure 2a shows the raypaths and wave vectors of a whistler-mode wave at frequency $\omega/\Omega_{e0} = 0.4$ in Models 1–3, where Ω_{e0} is the equatorial electron gyrofrequency at the wave launch point. The raypath (black solid line) of this wave falls closely along a magnetic field line (black dotted line) in each model. The wave vectors at different locations along the raypath are marked by the blue lines with arrows, which indicate both the magnitudes and
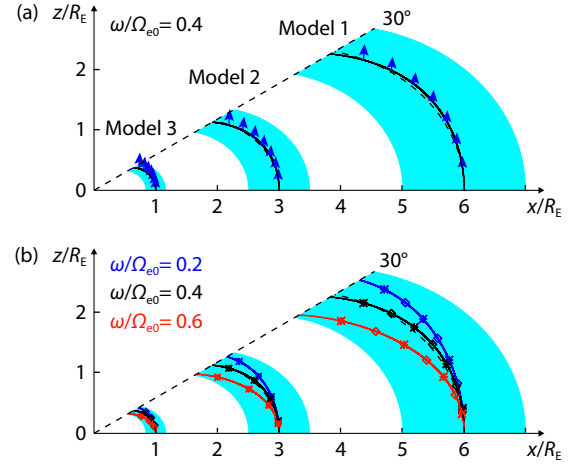

Figure 2. Propagation of whistler waves in different rescaled dipole magnetic fields. (a) Raypaths (black solid lines) and wave vectors (blue lines with arrows) of a whistler wave at $\omega/\Omega_{e0} = 0.4$ in the three models. (b) Raypaths (solid lines) of different-frequency waves in the three models. The locations (r, λ) on the raypaths in Model 2 (or Model 3) and their scaled-up locations $(\eta r, \lambda)$ in Model 1, marked by asterisks (or diamonds). The dotted curve indicates the magnetic field line.

directions of the wave vectors. During propagation toward higher latitudes, the wave vectors gradually increase and refract outward because of the dipole magnetic field. Figure 2b shows the raypaths (solid lines) of whistler-mode waves at different frequencies ($\omega/\Omega_{e0} = 0.2, 0.4, 0.6$) in the three models. Most obviously, the raypaths of different-frequency whistler waves are separate. The lower frequency wave ($\omega/\Omega_{e0} = 0.2$) propagates toward larger L, whereas the higher frequency wave ($\omega/\Omega_{e0} = 0.6$) propagates toward smaller L in all the models. This result is in agreement with previous theoretical and numerical works (Smith et al., 1960; Chen LJ et al., 2013, 2021). For each whistler-mode wave, the locations (r, λ) on its raypath in a scaled-down dipole field (Model 2 or Model 3) can be scaled up η times along the radial direction to obtain new locations $(\eta r, \lambda)$, marked by asterisks (or diamonds), which lie exactly on its raypath in a realistic dipole field (Model 1), as shown in Figure 2b. This result suggests that the raypath of a whistler-mode wave remains the same in different rescaled dipole fields.

Figure 3 shows the dependence of wave numbers and wave normal angles of whistler-mode waves on the magnetic latitude in the different rescaled dipole fields. The wave numbers of the whistler wave at $\omega/\Omega_{e0} = 0.4$ are equivalent at the same latitude in the different rescaled dipole fields (Figure 3a). Additionally, the wave normal angle θ as a function of the magnetic latitude remains the same in the different rescaled dipole fields for each whistler-mode wave. Therefore, the wave vectors are the same at the same magnetic latitude along the raypath in the different models. With the increase in magnetic latitude, the wave normal angle gradually increases, consistent with previous numerical works (Breuillard et al., 2012; Lu QM et al., 2019; Ke YG et al., 2022). Moreover, the higher frequency waves have larger wave normal angles than the lower frequency waves at the same latitude. For example, the wave at $\omega/\Omega_{e0} = 0.2$ has a wave normal angle of $\theta = 41°$, whereas the wave at $\omega/\Omega_{e0} = 0.6$ has a wave normal angle of $\theta = 59°$ at the latitude $\lambda = 15°$.
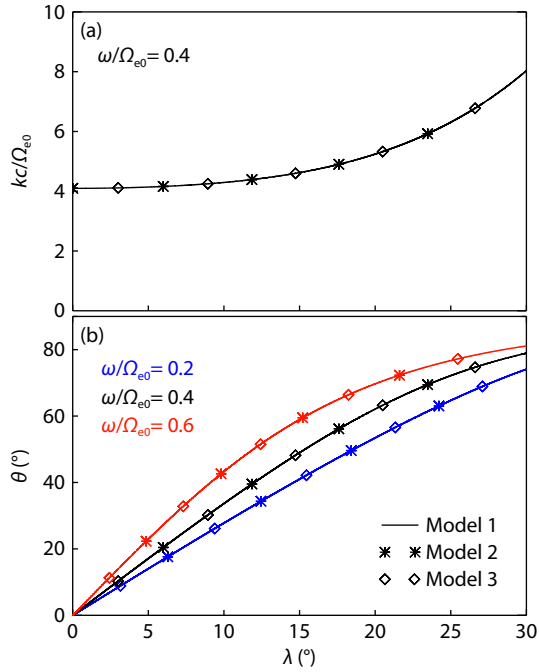
Figure 3. The dependence of wave numbers (a) and wave normal angles (b) of whistler waves on the magnetic latitude in different rescaled dipole fields (different models).

3.2 Wave Growth or Damping

We calculated the local growth rates along the wave raypath, based on a given hot electron distribution, and then estimated the wave growth or damping. In the simulation system, the parallel thermal velocity of hot electrons is set as $v_{\text{th}\parallel} = 0.2c$ (where c is the speed of light), and the temperature anisotropy at the equator is $T_{h\perp}/T_{h\parallel} = 3$. The hot electron density satisfies $n_h/n_{\text{eq}} = 0.01$. Figure 4 presents the growth rate, flight time, and relative amplitude of whistler-mode waves at different latitudes in the three models. For a whistler-mode wave at $\omega/\Omega_{e0} = 0.4$, its growth rate as a function of latitude remains the same in different rescaled dipole fields (Figure 4a), as do the waves at $\omega/\Omega_{e0} = 0.2$ and 0.6 (Figure 4b). However, the flight time of a whistler-mode wave is different when reaching the same latitude in the different rescaled dipole fields (Figure 4c). In a scaled-down dipole field with η (Model 2 or 3), the flight time is shorter than that in the realistic dipole field (Model 1), and the flight time multiplied by η times will be equal to that in the realistic dipole field (Figure 4d). Although the growth rates are identical, the wave gains are different because of the differences in flight time in the different rescaled dipole fields (Figure 4e). The wave amplification or attenuation in a scaled-down dipole field with η (Model 2 or 3) is smaller than that in the realistic dipole field (Model 1). And the relative amplitude B_w/B_{w0} raised to the power η will be equal to that in the realistic dipole field (Figure 4f), as expected by
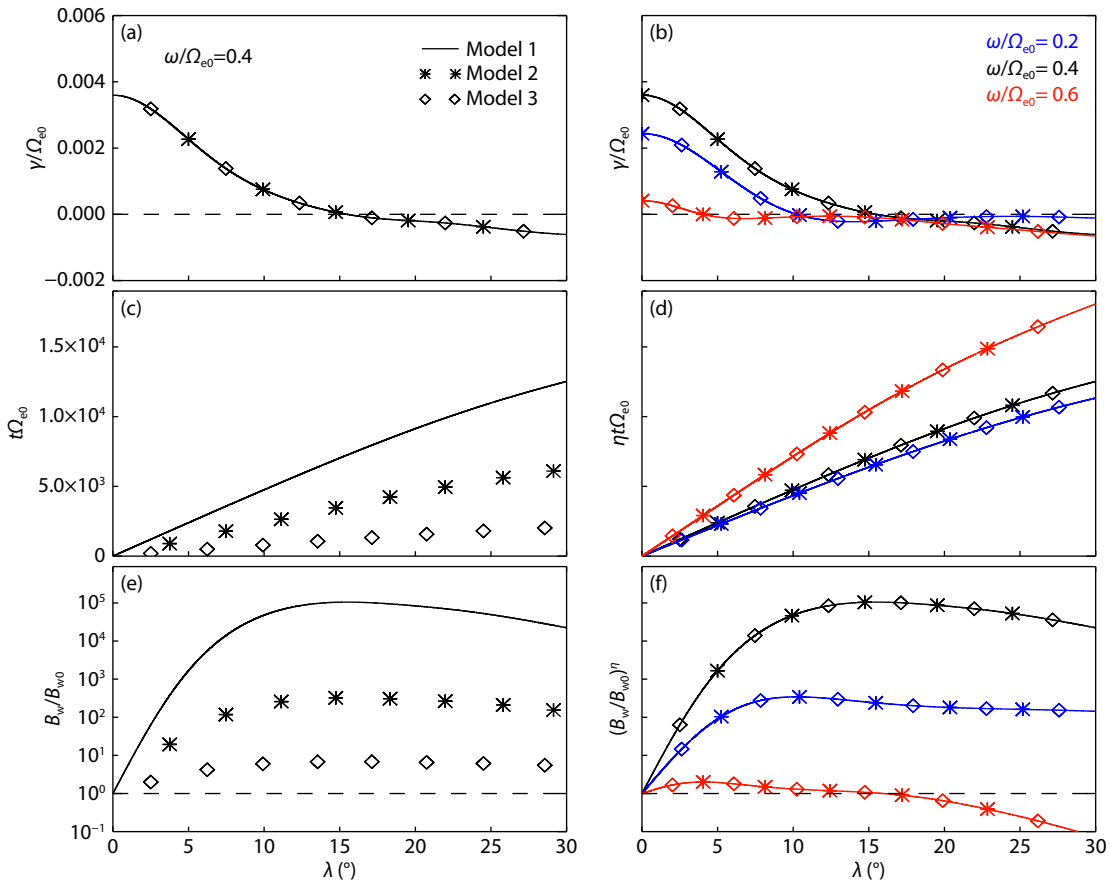

Figure 4. The wave growth or damping in different rescaled dipole fields. The growth rate (a), flight time (c), and relative amplitude (e) of a whistler wave at $\omega/\Omega_{e0} = 0.4$ at different latitudes in the three models. The growth rates (b), flight times multiplied by η (d), and relative amplitudes raised to the power of η (f) of different-frequency whistler waves at different latitudes in the three models.

Ke YG and Lu QM et al.: Simulations of whistler waves in rescaled dipole magnetic fields

Equation (1).

According to the above-mentioned results, to obtain the same wave gain in a scaled-down dipole field as that in the realistic dipole field, a simple approach is to increase the wave growth rate, which is proportional to the hot electron density. Therefore, we also traced a whistler-mode wave at $\omega/\Omega_{e0} = 0.4$ in Model 2 under $n_h/n_{eq} = 0.02$ and in Model 3 under $n_h/n_{eq} = 0.06$. The simulation results show that the growth rate of this wave in Model 2 (Model 3) is 2 (6) times larger than that in Model 1 with $n_h/n_{eq} = 0.01$ (Figure 5a). Although the flight times are different (Figure 5b), the relative amplitudes are the same in the three models (Figure 5c).

3.3 Wave Propagation in a Density Duct

The propagation of nonducted whistler-mode waves is explored in the previous sections. In addition, the propagation of whistler waves in an enhanced density duct in different rescaled dipole fields is studied. A density duct is embedded in the background density model (Equation (3)), which in the equatorial plane is described by a Gaussian function:

$$n_d = n_1 \exp\left[-\frac{(\eta L - \eta L_0)^2}{2\rho^2}\right], \tag{5}$$

where $n_1 = 2$ cm^{-3} is the density increase in the center of the duct, L_0 is the radial distance of the wave launch point, and $\rho = 0.07\ R_E$ is regarded as the half-width of the duct. The density profile is modified into

$$n_e = (n_{eq} + n_d)(\cos\lambda)^{-2a}, \tag{6}$$

which is shown in the different models in Figure 6.

Figure 7 shows the propagation characteristics of a whistler-mode wave at $\omega/\Omega_{e0} = 0.2$ in such a density duct in different rescaled dipole fields. Figure 7a shows that this wave trapped in the density duct propagates closely along the magnetic field line, unlike the nonducted wave (blue dotted line). Its wave normal angles fluctuate but remain quasi-parallel (Figure 7b), unlike that of the nonducted wave (blue dotted line). Moreover, the raypath
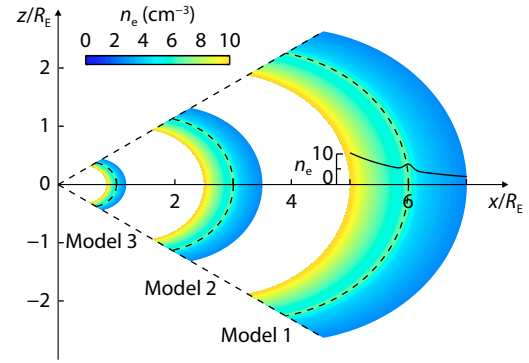
Figure 6. The distribution of the background electron density in the presence of an enhanced density duct in different rescaled dipole fields (different models).
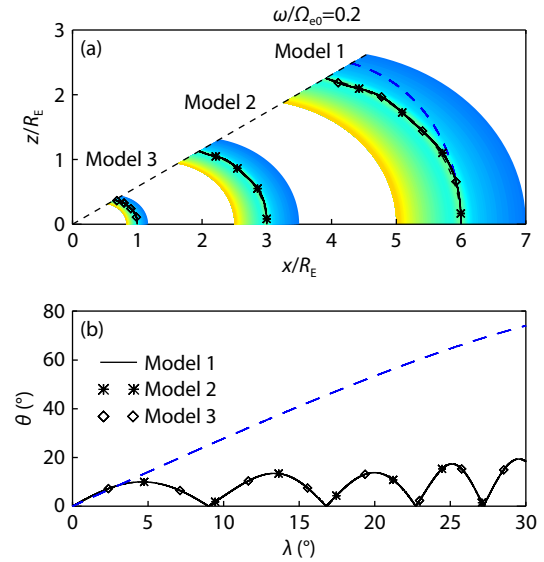
Figure 7. Propagation properties of a whistler wave in a density duct in different rescaled dipole fields. (a) Raypaths (solid lines) of a whistler wave at $\omega/\Omega_{e0} = 0.2$ in a density duct in different models. (b) The dependence of wave normal angles on the magnetic latitude in different models. The blue dotted lines indicate the raypaths (a) and wave normal angles (b) of the nonducted whistler wave at $\omega/\Omega_{e0} = 0.2$.
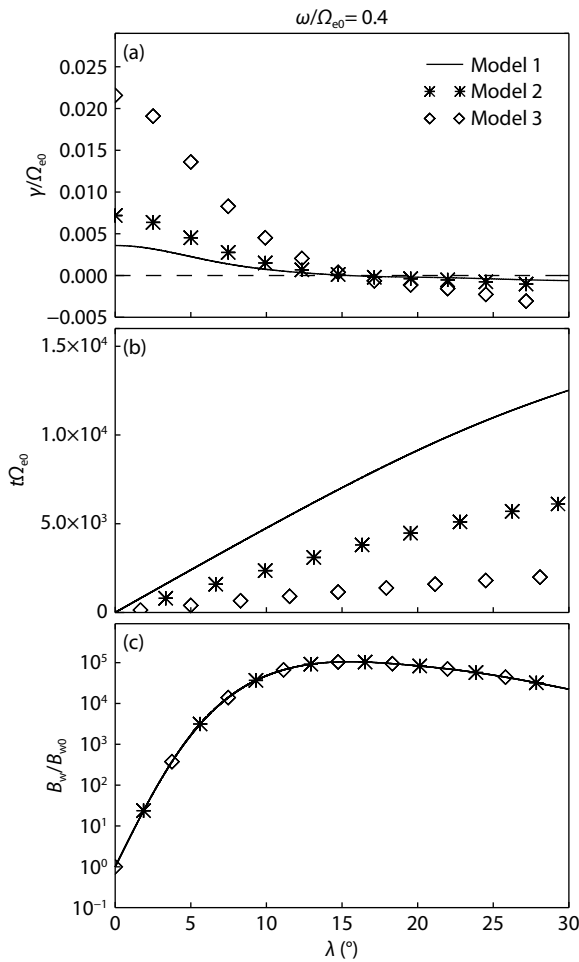

Figure 5. The growth rate (a), flight time (b), and relative amplitude (c) of a whistler wave at $\omega/\Omega_{e0} = 0.4$ at different latitudes in Model 1 under $n_h/n_{eq} = 0.01$, Model 2 under $n_h/n_{eq} = 0.02$, and Model 3 under $n_h/n_{eq} = 0.06$.

of this wave remains the same in different rescaled dipole fields (Figure 7a), as well as in the wave normal angles (Figure 7b). The growth rate, flight time, and relative amplitude of this wave in different rescaled dipole fields were also obtained but are not shown here because they follow the same pattern as those of the nonducted wave.

4. Discussion

In our ray-tracing simulations, the scaling factor η cannot be too large because the Wentzel–Kramers–Brillouin (WKB) approximation requires the wavelength to be much smaller than the characteristic scale of the plasma variation. The ray-tracing technique generally evaluates the wave growth or damping in a linear frame by integrating the linear growth rate along the wave raypath. However, a whistler-mode wave with sufficiently large amplitude may undergo remarkable nonlinear growth in a dipole magnetic field. Thus, the potential differences of whistler-mode waves in different rescaled dipole fields are also discussed in a nonlinear frame, as shown below.

The magnetic field inhomogeneity, $\frac{\partial \Omega_e}{\partial h}$, in a scaled-down dipole field with η is η times larger than that in a realistic dipole field (where Ω_e is the local electron gyrofrequency and h is the distance to the equator along the field line). Hence, the amplitude threshold for nonlinear growth (Omura et al., 2009; Kubota et al., 2018),

$$B_{th} = \frac{A}{n_h^2}\left(\frac{\partial^2 \Omega_e}{\partial h^2}\right)^2,\qquad(7)$$

in this scaled-down dipole field is η^4 times larger than that in the realistic dipole field. Here, A is a coefficient that is nearly the same in different rescaled dipole fields. However, the magnetic field inhomogeneity is not included in the formula for the nonlinear growth rate (Omura et al., 2009),

$$\Gamma_N = B\frac{n_h}{\sqrt{B_w}},\qquad(8)$$

where B is a coefficient that is nearly the same in the different rescaled dipole fields. The nonlinear growth rate Γ_N is proportional to the hot electron density. Note that the nonlinear growth rate is obtained by assuming the wave is parallel, which may no longer apply to the waves when they become oblique. Obviously, increasing the hot electron density in a scaled-down dipole field can not only drop the amplitude threshold B_{th} but also increase the nonlinear growth rate. Therefore, increasing the hot electron density in a scaled-down dipole field is a useful approach that brings the wave propagation closer to that in a realistic dipole field. Our study offers important guidance for kinetic simulations of whistler-mode waves.

5. Conclusions

To study the generation and propagation of whistler-mode waves in the Earth's inner magnetosphere, many kinetic simulations have been carried out by using a scaled-down dipole magnetic field to save computational time. To determine whether whistler wave propagation in the scaled-down dipole field is consistent with that in the realistic dipole field, we developed a 2-D ray-tracing code to investigate the propagation of whistler-mode waves in different rescaled dipole fields. The following conclusions were drawn:

(1) A 2-D ray-tracing code with a scalable dipole magnetic field was developed to study the propagation of whistler-mode waves in different rescaled dipole magnetic fields.

(2) Parallel whistler waves at higher frequencies tend to have larger wave normal angles at the same latitude after leaving the magnetic equator.

(3) The raypaths and wave normal angles of whistler-mode waves in a scaled-down dipole field are the same as those in the realistic dipole field.

(4) Compared with the wave gain in the realistic dipole field, the amplification or attenuation of a whistler wave is smaller because of the shorter propagation time in the scaled-down dipole field.

References

Agapitov, O., Krasnoselskikh, V., Khotyaintsev, Y. V., and Rolland, G. (2011). A statistical study of the propagation characteristics of whistler waves observed by Cluster. *Geophys. Res. Lett.*, *38*(20), L20103. https://doi.org/10.1029/2011GL049597

Agapitov, O., Artemyev, A., Krasnoselskikh, V., Khotyaintsev, Y. V., Mourenas, D., Breuillard, H., Balikhin, M., and Rolland, G. (2013). Statistics of whistler mode waves in the outer radiation belt: cluster STAFF-SA measurements. *J. Geophys. Res.: Space Phys.*, *118*(6), 3407–3420. https://doi.org/10.1002/jgra.50312

Anderson, R. R., and Maeda, K. (1977). VLF emissions associated with enhanced magnetospheric electrons. *J. Geophys. Res.*, *82*(1), 135–146. https://doi.org/10.1029/JA082i001p00135

Artemyev, A., Agapitov, O., Mourenas, D., Krasnoselskikh, V., Shastun, V., and Mozer, F. (2016). Oblique whistler-mode waves in the Earth's inner magnetosphere: energy distribution, origins, and role in radiation belt dynamics. *Space Sci. Rev.*, *200*(1-4), 261–355. https://doi.org/10.1007/s11214-016-0252-5

Bortnik, J., Inan, U. S., and Bell, T. F. (2003). Energy distribution and lifetime of magnetospherically reflecting whistlers in the plasmasphere. *J. Geophys. Res.: Space Phys.*, *108*(A5), 1199. https://doi.org/10.1029/2002JA009316

Bortnik, J., Thorne, R. M., and Meredith, N. P. (2008). The unexpected origin of plasmaspheric hiss from discrete chorus emissions. *Nature*, *452*(7183), 62–66. https://doi.org/10.1038/nature06741

Breuillard, H., Zaliznyak, Y., Krasnoselskikh, V., Agapitov, O., Artemyev, A., and Rolland, G. (2012). Chorus wave-normal statistics in the Earth's radiation belts from ray tracing technique. *Ann. Geophys.*, *30*(8), 1223–1233. https://doi.org/10.5194/angeo-30-1223-2012

Brinca, A. L. (1972). On the stability of obliquely propagating whistlers. *J. Geophys. Res.*, *77*(19), 3495–3507. https://doi.org/10.1029/JA077i019p03495

Burtis, W. J., and Helliwell, R. A. (1969). Banded chorus—A new type of VLF radiation observed in the magnetosphere by OGO 1 and OGO 3. *J. Geophys. Res.*, *74*(11), 3002–3010. https://doi.org/10.1029/JA074i011p03002

Burtis, W. J., and Helliwell, R. A. (1976). Magnetospheric chorus: Occurrence patterns and normalized frequency. *Planet. Space Sci.*, *24*(11), 1007–1024. https://doi.org/10.1016/0032-0633(76)90119-7

Carpenter, D. L., and Anderson, R. R. (1992). An ISEE/whistler model of equatorial electron density in the magnetosphere. *J. Geophys. Res.: Space Phys.*, *97*(A2), 1097–1108. https://doi.org/10.1029/91ja01548

Chan, K. W., and Holzer, R. E. (1976). ELF hiss associated with plasma density enhancements in the outer magnetosphere. *J. Geophys. Res.*, *81*(13), 2267–2274. https://doi.org/10.1029/JA081i013p02267

Chen, H. Y., Gao, X. L., Lu, Q. M., Sauer, K., Chen, R., Yao, J. S., and Wang, S. (2021). Gap formation around $0.5\Omega_e$ of whistler-mode waves excited by electron temperature anisotropy. *J. Geophys. Res.: Space Phys.*, *126*(2), e2020JA028631. https://doi.org/10.1029/2020ja028631

Chen, H. Y., Gao, X. L., Lu, Q. M., Fan, K., Ke, Y. G., Wang, X. Y., and Wang, S. (2022). Gap formation around $0.5\Omega_e$ in the whistler-mode waves due to the plateau-like shape in the parallel electron distribution: 2D PIC simulations. *J. Geophys. Res.: Space Phys.*, *127*(5), e2021JA030119. https://doi.org/10.1029/2021ja030119

Chen, L. J., Bortnik, J., Thorne, R. M., Horne, R. B., and Jordanova, V. K. (2009). Three-dimensional ray tracing of VLF waves in a magnetospheric environment containing a plasmaspheric plume. *Geophys. Res. Lett.*, *36*(22), L22101. https://doi.org/10.1029/2009gl040451

Chen, L. J., Thorne, R. M., Jordanova, V. K., Wang, C. P., Gkioulidou, M., Lyons, L., and Horne, R. B. (2010). Global simulation of EMIC wave excitation during the 21 April 2001 storm from coupled RCM-RAM-HOTRAY modeling. *J. Geophys. Res.: Space Phys.*, *115*(A7), A07209. https://doi.org/10.1029/2009JA015075

Chen, L. J., Thorne, R. M., Li, W., and Bortnik, J. (2013). Modeling the wave normal distribution of chorus waves. *J. Geophys. Res.: Space Phys.*, *118*(3), 1074–1088. https://doi.org/10.1029/2012ja018343

Chen, L. J., Zhang, X. J., Artemyev, A., Zheng, L. H., Xia, Z. Y., Breneman, A. W., and Horne, R. B. (2021). Electron microbursts induced by nonducted chorus waves. *Front. Astron. Space Sci.*, *8*, 745927. https://doi.org/10.3389/fspas.2021.745927

Da Silva, C. L., Wu, S., Denton, R. E., Hudson, M. K., and Millan, R. M. (2017). Hybrid fluid-particle simulation of whistler-mode waves in a compressed dipole magnetic field: implications for dayside high-latitude chorus. *J. Geophys. Res.: Space Phys.*, *122*(1), 432–448. https://doi.org/10.1002/2016ja023446

Décréau, P. M. E., Béghin, C., and Parrot, M. (1982). Global characteristics of the cold plasma in the equatorial plasmapause region as deduced from the Geos 1 Mutual Impedance Probe. *J. Geophys. Res.: Space Phys.*, *87*(A2), 695–712. https://doi.org/10.1029/JA087iA02p00695

Deng, Z. K., Xiao, F. L., Zhou, Q. H., Zhang, S., Liu, S., Yang, Q. W., Tang, J. W., Kumamoto, A., Miyoshi, Y., … Nakamura, S. (2022). Direct evidence for auroral kilometric radiation propagation into radiation belts based on Arase spacecraft and Van Allen Probe B. *Geophys. Res. Lett.*, *49*(19), e2022GL100860. https://doi.org/10.1029/2022GL100860

Denton, R. E., Goldstein, J., and Menietti, J. D. (2002). Field line dependence of magnetospheric electron density. *Geophys. Res. Lett.*, *29*(24), 2205. https://doi.org/10.1029/2002GL015963

Denton, R. E., Takahashi, K., Galkin, I. A., Nsumei, P. A., Huang, X., Reinisch, B. W., Anderson, R. R., Sleeper, M. K., and Hughes, W. J. (2006). Distribution of density along magnetospheric field lines. *J. Geophys. Res.: Space Phys.*, *111*(A4), A04213. https://doi.org/10.1029/2005JA011414

Gao, X. L., Li, W., Thorne, R. M., Bortnik, J., Angelopoulos, V., Lu, Q. M., Tao, X., and Wang S. (2014). New evidence for generation mechanisms of discrete and hiss-like whistler mode waves. *Geophys. Res. Lett.*, *41*(14), 4805–4811. https://doi.org/10.1002/2014gl060707

Gao, X. L., Chen, L. J., Li, W., Lu, Q. M., and Wang, S. (2019). Statistical results of the power gap between lower-band and upper-band chorus waves. *Geophys. Res. Lett.*, *46*(8), 4098–4105. https://doi.org/10.1029/2019gl082140

Gao, X. L., Chen, R., Lu, Q. M., Chen, L. J., Chen, H. Y., and Wang, X. Y. (2022). Observational evidence for the origin of repetitive chorus emissions. *Geophys. Res. Lett.*, *49*(12), e2022GL099000. https://doi.org/10.1029/2022GL099000

Guo, M. Y., Zhou, Q. H., Xiao, F. L., Liu, S., He, Y. H., and Yang, C. (2020). Upward propagation of lightning-generated whistler waves into the radiation belts. *Sci. China Technol. Sci.*, *63*(2), 243–248. https://doi.org/10.1007/s11431-018-9486-9

Haselgrove, J. (1955). Ray theory and a new method for ray tracing. Cambridge, UK: Physics of the Ionosphere Conference (pp. 355–364), Cavendish Laboratory

Hikishima, M., and Omura, Y. (2012). Particle simulations of whistler-mode rising-tone emissions triggered by waves with different amplitudes. *J. Geophys. Res.: Space Phys.*, *117*(A4), A04226. https://doi.org/10.1029/2011ja017428

Horne, R. B. (1989). Path-integrated growth of electrostatic waves: the generation of terrestrial myriametric radiation. *J. Geophys. Res.: Space Phys.*, *94*(A7), 8895–8909. https://doi.org/10.1029/JA094iA07p08895

Horne, R. B., and Thorne, R. M. (1998). Potential waves for relativistic electron scattering and stochastic acceleration during magnetic storms. *Geophys. Res. Lett.*, *25*(15), 3011–3014. https://doi.org/10.1029/98GL01002

Horne, R. B., Thorne, R. M., Shprits, Y. Y., Meredith, N. P., Glauert, S. A., Smith, A. J., Kanekal, S. G., Baker, D. N., Engebretson, M. J., … Decreau, P. M. E. (2005). Wave acceleration of electrons in the Van Allen radiation belts. *Nature*, *437*(7056), 227–230. https://doi.org/10.1038/nature03939

Kang, N., Bortnik, J., An, X., and Claudepierre, S. G. (2021). Propagation of chorus waves generated in minimum-B pockets. *Geophys. Res. Lett.*, *48*(24), e2021GL096478. https://doi.org/10.1029/2021gl096478

Kasahara, S., Miyoshi, Y., Yokota, S., Mitani, T., Kasahara, Y., Matsuda, S., Kumamoto, A., Matsuoka, A., Kazama, Y., … Shinohara, I. (2018). Pulsating aurora from electron scattering by chorus waves. *Nature*, *554*(7692), 337–340. https://doi.org/10.1038/nature25505

Katoh, Y., and Omura, Y. (2006). A study of generation mechanism of VLF triggered emission by self-consistent particle code. *J. Geophys. Res.: Space Phys.*, *111*(A12), A12207. https://doi.org/10.1029/2006ja011704

Katoh, Y., and Omura, Y. (2007). Computer simulation of chorus wave generation in the Earth's inner magnetosphere. *Geophys. Res. Lett.*, *34*(3), L03102. https://doi.org/10.1029/2006gl028594

Ke, Y. G., Gao, X. L., Lu, Q. M., Wang, X. Y., and Wang, S. (2017). Generation of rising-tone chorus in a two-dimensional mirror field by using the general curvilinear PIC code. *J. Geophys. Res.: Space Phys.*, *122*(8), 8154–8165. https://doi.org/10.1002/2017ja024178

Ke, Y. G., Lu, Q. M., Gao, X. L., Wang, X. Y., Chen, L. J., Wang, S. J., and Wang, S. (2020). Particle-in-cell simulations of characteristics of rising-tone chorus waves in the inner magnetosphere. *J. Geophys. Res.: Space Phys.*, *125*(7), e2020JA027961. https://doi.org/10.1029/2020ja027961

Ke, Y. G., Chen, L. J., Gao, X. L., Lu, Q. M., Wang, X. Y., Chen, R., Chen, H. Y., and Wang, S. (2021). Whistler-mode waves trapped by density irregularities in the Earth's magnetosphere. *Geophys. Res. Lett.*, *48*(7), e2020GL092305. https://doi.org/10.1029/2020gl092305

Ke, Y. G., Gao, X. L., Lu, Q. M., Wang, X. Y., Chen, R., Chen, H. Y., and Wang, S. (2022). Deformation of electron distributions due to Landau trapping by the whistler-mode wave. *Geophys. Res. Lett.*, *49*(3), e2021GL096428. https://doi.org/10.1029/2021GL096428

Kennel, C. (1966). Low-frequency whistler mode. *Phys. Fluids*, *9*(11), 2190–2202. https://doi.org/10.1063/1.1761588

Kennel, C. F., and Petschek, H. E. (1966). Limit on stably trapped particle fluxes. *J. Geophys. Res.*, *71*(1), 1–28. https://doi.org/10.1029/JZ071i001p00001

Kimura, I. (1966). Effects of ions on whistler-mode ray tracing. *Radio Sci.*, *1*(3), 269–284. https://doi.org/10.1002/rds196613269

Kubota, Y., Omura, Y., Kletzing, C., and Reeves, G. (2018). Generation process of large-amplitude upper-band chorus emissions observed by Van Allen probes. *J. Geophys. Res.: Space Phys.*, *123*(5), 3704–3713. https://doi.org/10.1029/2017ja024782

LeDocq, M. J., Gurnett, D. A., and Hospodarsky, G. B. (1998). Chorus source locations from VLF Poynting flux measurements with the Polar spacecraft. *Geophys. Res. Lett.*, *25*(21), 4063–4066. https://doi.org/10.1029/1998GL900071

Li, W., Thorne, R. M., Angelopoulos, V., Bonnell, J. W., McFadden, J. P., Carlson, C. W., LeContel, O., Roux, A., Glassmeier, K. H., and Auster, H. U. (2009). Evaluation of whistler-mode chorus intensification on the nightside during an injection event observed on the THEMIS spacecraft. *J. Geophys. Res.: Space Phys.*, *114*(A1), A00C14. https://doi.org/10.1029/2008JA013554

Li, W., Bortnik, J., Thorne, R. M., and Angelopoulos, V. (2011). Global distribution of wave amplitudes and wave normal angles of chorus waves using THEMIS wave observations. *J. Geophys. Res.: Space Phys.*, *116*(A12), A12205. https://doi.org/10.1029/2011ja017035

Li, W., Thorne, R. M., Bortnik, J., Tao, X., and Angelopoulos, V. (2012). Characteristics of hiss-like and discrete whistler-mode emissions. *Geophys. Res. Lett.*, *39*(18), L18106. https://doi.org/10.1029/2012gl053206

Li, W., Bortnik, J., Thorne, R. M., Cully, C. M., Chen, L. J., Angelopoulos, V., Nishimura, Y., Tao, J. B., Bonnell, J. W., and LeContel, O. (2013). Characteristics of the Poynting flux and wave normal vectors of whistler-mode waves observed on THEMIS. *J. Geophys. Res.: Space Phys.*, *118*(4), 1461–1471. https://doi.org/10.1002/jgra.50176

Lu, Q. M., Ke, Y. G., Wang, X. Y., Liu, K. J., Gao, X. L., Chen, L. J., and Wang, S. (2019). Two-dimensional gcPIC simulation of rising-tone chorus waves in a dipole magnetic field. *J. Geophys. Res.: Space Phys.*, *124*(6), 4157–4167. https://doi.org/10.1029/2019ja026586

Lu, Q. M., Chen L. J., Wang, X. Y., Gao, X. L., Lin, Y., and Wang, S. (2021). Repetitive emissions of rising-tone chorus waves in the inner magnetosphere. *Geophys. Res. Lett.*, *48*(15), e2021GL094979. https://doi.org/10.1029/2021gl094979

Meredith, N. P., Horne, R. B., Kersten, T., Li, W., Bortnik, J., Sicard, A., and Yearby, K. H. (2018). Global model of plasmaspheric hiss from multiple satellite observations. *J. Geophys. Res.: Space Phys.*, *123*(6), 4526–4541. https://doi.org/10.1029/2018JA025226

Ni, B. B., Thorne, R. M., Shprits, Y. Y., and Bortnik, J. (2008). Resonant scattering of plasma sheet electrons by whistler-mode chorus: contribution to diffuse auroral precipitation. *Geophys. Res. Lett.*, *35*(11), L11106. https://doi.org/10.1029/2008GL034032

Nishimura, Y., Bortnik, J., Li, W., Thorne, R. M., Lyons, L. R., Angelopoulos, V., Mende, S. B., Bonnell, J. W., Le Contel, O., … Auster, U. (2010). Identifying the driver of pulsating aurora. *Science*, *330*(6000), 81–84. https://doi.org/10.1126/science.1193186

Nunn, D., and Omura, Y. (2012). A computational and theoretical analysis of falling frequency VLF emissions. *J. Geophys. Res.: Space Phys.*, *117*(A8), A08228. https://doi.org/10.1029/2012ja017557

Omura, Y., Katoh, Y., and Summers, D. (2008). Theory and simulation of the generation of whistler-mode chorus. *J. Geophys. Res.: Space Phys.*, *113*(A4), A04223. https://doi.org/10.1029/2007ja012622

Omura, Y., Hikishima, M., Katoh, Y., Summers, D., and Yagitani, S. (2009). Nonlinear mechanisms of lower-band and upper-band VLF chorus emissions in the magnetosphere. *J. Geophys. Res.: Space Phys.*, *114*(A7), A07217. https://doi.org/10.1029/2009ja014206

Omura, Y., and Nunn, D. (2011). Triggering process of whistler mode chorus emissions in the magnetosphere. *J. Geophys. Res.: Space Phys.*, *116*(A5), A05205. https://doi.org/10.1029/2010ja016280

Reeves, G. D., Spence, H. E., Henderson, M. G., Morley, S. K., Friedel, R. H. W., Funsten, H. O., Baker, D. N., Kanekal, S. G., Blake, J. B., … Niehof, J. T. (2013). Electron acceleration in the heart of the Van Allen radiation belts. *Science*, *341*(6149), 991–994. https://doi.org/10.1126/science.1237743

Rönnmark, K. (1982). WHAMP: waves in homogeneous, anisotropic, multicomponent plasmas. Kiruna, Sweden: Kiruna Geophysical Institute.

Santolík, O., Gurnett, D. A., Pickett, J. S., Parrot, M., and Cornilleau-Wehrlin, N. (2005). Central position of the source region of storm-time chorus. *Planet. Space Sci.*, *53*(1-3), 299–305. https://doi.org/10.1016/j.pss.2004.09.056

Sauer, K., Baumgärtel, K., and Sydora, R. (2020). Gap formation around $\Omega_e/2$ and generation of low-band whistler waves by Landau-resonant electrons in the magnetosphere: Predictions from dispersion theory. *Earth Planet. Phys.*, *4*(2), 138–150. https://doi.org/10.26464/epp2020020

Smith, R. L., Helliwell, R. A., and Yabroff, I. W. (1960). A theory of trapping of whistlers in field-aligned columns of enhanced ionization. *J. Geophys. Res.*, *65*(3), 815–823. https://doi.org/10.1029/JZ065i003p00815

Stix, T. H. (1992). *Waves in Plasmas*. Melville, NY: American Institute of Physics.

Su, Z. P., Liu, N. G., Zheng, H. N., Wang, Y. M., and Wang, S. (2018). Large-amplitude extremely low frequency hiss waves in plasmaspheric plumes. *Geophys. Res. Lett.*, *45*(2), 565–577. https://doi.org/10.1002/2017GL076754

Summers, D., Omura, Y., Miyashita, Y., and Lee, D. H. (2012). Nonlinear spatiotemporal evolution of whistler mode chorus waves in Earth's inner magnetosphere. *J. Geophys. Res.: Space Phys.*, *117*(A9), A09206. https://doi.org/10.1029/2012ja017842

Tao, X., Zonca, F., Chen, L. J., and Wu, Y. F. (2020). Theoretical and numerical studies of chorus waves: a review. *Sci. China Earth Sci.*, *63*(1), 78–92. https://doi.org/10.1007/s11430-019-9384-6

Thorne, R. M., Smith, E. J., Burton, R. K., and Holzer, R. E. (1973). Plasmaspheric hiss. *J. Geophys. Res.*, *78*(10), 1581–1596. https://doi.org/10.1029/JA078i010p01581

Thorne, R. M., Ni, B. B., Tao, X., Horne, R. B., and Meredith, N. P. (2010). Scattering by chorus waves as the dominant cause of diffuse auroral precipitation. *Nature*, *467*(7318), 943–946. https://doi.org/10.1038/nature09467

Thorne, R. M., Li, W., Ni, B., Ma, Q., Bortnik, J., Chen, L., Baker, D. N., Spence, H. E., Reeves, G. D., … Kanekal, S. G. (2013). Rapid local acceleration of relativistic radiation-belt electrons by magnetospheric chorus. *Nature*, *504*(7480), 411–414. https://doi.org/10.1038/nature12889

Tsurutani, B. T., and Smith, E. J. (1974). Postmidnight chorus: a substorm phenomenon. *J. Geophys. Res.*, *79*(1), 118–127. https://doi.org/10.1029/JA079i001p00118

Tsurutani, B. T., and Smith, E. J. (1977). Two types of magnetospheric ELF chorus and their substorm dependences. *J. Geophys. Res.*, *82*(32), 5112–5128. https://doi.org/10.1029/JA082i032p05112

Xiao, F. L., Zhou, Q. H., Su, Z. P., He, Z. G., Yang, C., Liu, S., He, Y. H., and Gao, Z. L. (2016). Explaining occurrences of auroral kilometric radiation in Van Allen radiation belts. *Geophys. Res. Lett.*, *43*(23), 11971–11978. https://doi.org/10.1002/2016GL071728